# Organozinc reagents in solution: insights from ab initio molecular dynamics and X-ray absorption spectroscopy

Jordan Rio, Quentin Pessemesse, Michele Cascella, Pierre-Adrien Payard, Marie-Eve L Perrin

# Organozinc reagents in solution: insights from *ab initio* molecular dynamics and X-ray absorption spectroscopy

Jordan Rio,[a] Quentin Pessemesse,[a] Michele Cascella,[b] Pierre-Adrien Payard*[a,‡] and Marie-Eve L. Perrin*[a]

Organozinc reagents play a critical role in synthesis, yet our comprehension of their structure-reactivity relationships is limited by a lack of information about their structures in solution. This study introduces a computational workflow, validated by X-ray absorption spectroscopy, to investigate organozinc reagents in solution. The solvation states of $ZnCl_2$, ZnMeCl and $ZnMe_2$ were explored using ab initio molecular dynamics (metadynamics and Blue Moon sampling) within an explicit solvent cage. The study revealed the existence of various solvation states at room temperature, providing clarity on the previously debated structure of $ZnMe_2$ in THF solution. These findings were confirmed by near-edge X-ray absorption spectroscopy (XANES) interpreted using time-dependent density functional theory (TD-DFT) calculations.

## Introduction

Organozinc compounds are ubiquitous reagents in synthesis with applications ranging from polymer synthesis to pharmaceutical and crop chemistry.[1] They are involved in reactions such as halogen/metal exchanges,[2] conjugate additions[3] and the Negishi cross-coupling.[4,5] Their sensitivity to chemical environment, such as solvents and additives, enables a fine tuning of their reactivity compared to that of more polar organometallic compounds.[6] The crucial role played by solvent mixtures in stabilizing organozinc intermediates involved in Pd-catalysed Negishi cross-coupling has been highlighted by the group of Organ.[7–12] The group of Blum revealed such effects on the synthesis of organozinc compounds from Zn(0).[13–15] Obtaining relevant information from molecular modelling on organozinc compounds requires a proper description of the chemical environment.

In addition, the choice of the solvent model proved critical to study the speciation of organozinc compounds in solution.[16–18] Even though continuum solvent models alone were reported as non suitable to describe organozinc solvation (Tables S1-S2),[16,19] microsolvation approaches barely improve the model as the number of solvent molecules coordinated to zinc is variable and unknown. In the latter case, estimating solvation entropy variations along reaction pathways remains a challenge despite the many reported corrections.[20–23] Hence, an explicit depiction of all solvation shells is required to model organozinc reagents in solution. An *ab initio* molecular dynamic approach is appealing as it

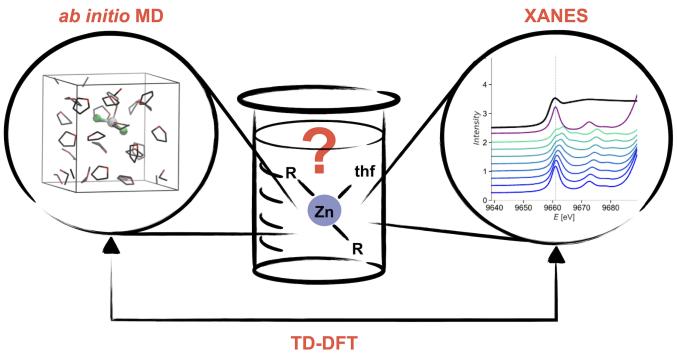


Fig. 1 Proposed joined theoretical and experimental approach to unveil the solvation states of zinc compounds in thf.

both accurately accounts for solvation entropy and enables sampling of the solute's solvation states. However, free energy surface exploration with molecular dynamics is painstakingly slow at the DFT level. A bias is thus needed to accelerate the sampling of solvation states. A history-dependent bias, as implemented in metadynamics, is incrementally deposited to drive the explo-

[a] *Universite Claude Bernard Lyon 1, CNRS, CPE-Lyon, UMR 5246, ICBMS, 1 rue Victor Grignard, F-69622 Villeurbanne cedex, France ; Tel: +33 472 448 168; E-mail: pierre-adrien.payard@univ-lyon1.fr; marie-eve.perrin@univ-lyon1.fr*

[b] *Department of Chemistry and Hylleraas Centre for Quantum Molecular Sciences, University of Oslo, P.O. Box 1033 Blindern, 0315 Oslo, Norway*

† Electronic Supplementary Information (ESI) available: experimental procedures, additional modelling and spectroscopic data, templates of CP2K and ORCA inputs, initial XYZ geometries used for Blue Moon simulations, raw XAS data. See DOI: 00.0000/00000000.

‡ Present address: Dunia Innovations, Rheinsberger Str.76/77, 10115 Berlin, Germany.

ration of the free energy surface along a reaction coordinate that is described as a set of relevant collective variables.[24–26] Compared to unbiased molecular dynamics, metadynamics promotes the occurrence of rare events, without prior knowledge of the surface. The free energy surface can then be reconstructed from the history-dependent bias. This approach provided valuable insight on the solvation of the $Na^+$ ion in tetrahydrofuran (thf) solution,[27] on the dynamic structure of Grignard and turbo-Grignard reagents,[28–30] and on the speciation of $ZnCl_2$ in water.[31] However, convergence of the metadynamics free energy surface is slow which prevents its quantitative interpretation. Based on structures sampled with metadynamics, thermodynamic integration in the Blue Moon ensemble,[32] using a monodimensional reaction coordinate, ensures a fast and well-behaved convergence. Thus, accessing quantitative information on the solvation thermodynamics and kinetics of organozinc reagents becomes possible.

Experimentally, the determination of the solvation states of organozinc compounds is as challenging as their computational prediction. Proposed solvation states usually rely on solid-state X-ray diffraction structures. Such structures have been reported for zinc chloride, bis(pentafluorophenyl)zinc and bisfluoroenylzinc,[33,34] in which Zn has a distorted tetrahedral geometry with two thf molecules. Solvated Zn-Mg aggregates and ion pairs were also reported by the group of Hevia.[35,36]

However, these solid state structures are not necessarily representative of structures in solution and are scarce, except for a handful of polar zinc complexes.[6] Evaluating a solvent model using *in situ* spectroscopic data is delicate because of fast equilibria between solvation states resulting in averaged spectroscopic signatures. For instance, routine $^1$H NMR spectroscopy provides ambiguous information about the solvation state of $ZnMe_2$, which shows up as a singlet (Figure S4). This could be interpreted as the absence of coordinated solvent molecules, as multiple coordination states in fast exchange or as oligomerisation.[16] *In fine*, currently available experimental data concerning organozincs solvation remains patchy.[37,38] The group of Espinet studied the solvation of dimethylzinc and zinc dichloride in solution experimentally and computationally.[16] Based on microcalorimetric monitoring of stoichiometric mixtures of pure $ZnMe_2$ and thf, and subsequent dilution, they proposed the exothermic coordination of $ZnMe_2$ by two thf molecules ($\Delta_{solv}H^\circ = -7.9 \pm 0.4$ kcal mol$^{-1}$). However, this enthalpy accounts for both the coordination and the mixing (excess) contributions. This solvation state assignment also contrasts from earlier computational report that highlighted the poor electrophilicity of metal center in $ZnMe_2$ relative to ZnMeCl,[39,40] $ZnMe_2$ being coordinated by strongly coordinating ligand such as TMEDA.[41]

A possible way to unambiguously characterize the averaged coordination shells of Zn under dilute conditions is X-ray absorption spectroscopy (XAS). XAS measures the absorption resulting from the excitation of tightly bound core electrons. In the 10-150 eV range above the chemical potential (X-ray Absorption Near-Edge Structure – XANES), the core electron is excited to vacant orbitals. XANES is generally used to identify the surrounding symmetry and oxydation state of an element. At more than 150 eV above chemical potential (Extended X-ray Absorption Fine Structure – EXAFS), the scattering of the photoelectron informs on the local atomic structure, such as coordination number, distances and thermal disorder.[42] EXAFS has been used by the group of Lei to support hypotheses on the structure of zinc halides, organozincates and organocuprates in thf solution.[43,44] Additionally, the solvation states of metal ions in aqueous solutions were elucidated by comparing recorded EXAFS spectra to those simulated from *ab initio* molecular dynamics. This comparison has demonstrated that explicit solvent models are relevant to compute this spectroscopic signatures.[45–48] However, some limitations of EXAFS arise with solvated organometallic complexes due to the similar backscattering of C and O atoms, which hampers reliable linear combination fits. Interpreting XANES at the molecular level is challenging, although its spectroscopic signature remains information-rich. For example, XANES at the Zn K-edge has been used recently in combination with $^{31}$P NMR to gain insight into the involvement of diphosphine ligands on the formation of Fe-Zn heterobimetallic species in the iron-catalysed Negishi reaction.[49]

Herein, we propose an innovative approach to determine the solvation states of organozinc compounds in thf solutions. This approach is based on metadynamics exploration, followed by thermodynamic integration in the Blue Moon ensemble, and rationalisation of the XANES signature at the zinc K-edge thanks to computed spectra. The resulting methodology is a straightforward means to probe the solvation behavior of organometallic systems in organic solvents.

## Computational strategy and details

### Preliminary exploration with metadynamics

All simulations were carried out in $15 \times 15 \times 15$ Å$^3$ cubic cells, containing 25 thf molecules and one solute molecule (Figure 2) corresponding to a solute concentration of 0.45 mol L$^{-1}$. The cells were generated using the Packmol software.[50] All molecular dynamic simulations were performed using the revised PBE functional[51,52] with the D3BJ empirical dispersion correction as implemented in the CP2k software.[53–55] The Gaussian-Plane-Wave scheme was used,[56] with double-$\zeta$ quality MOLOPT basis sets,[57] their associated Goedecker-Teter-Hutter (GTH) effective core potentials,[58] and a plane wave cutoff of 500 Ry. For each simulation, the temperature was equilibrated during 5 ps of free *ab initio* molecular dynamics prior to *ab initio* metadynamic simulations. Free-energy surfaces were explored using the coordination numbers of Zn to X (X = O, Cl, Me) as defined within Equation 1:

$$CN[\mathrm{Zn-X}] = \sum_i \frac{1-\left(\frac{r_i}{r_0}\right)^{NN}}{1-\left(\frac{r_i}{r_0}\right)^{ND}} \quad (1)$$

where $r_i$ is the Zn–X distance, $r_0$ is an estimated Zn–X distance at the transition state (for X = Me, O: $r_i$ = 2.6 Å, for X = Cl: $r_i$ = 2.8 Å), and $NN$ and $ND$ are smoothing empirical coefficients ($NN$ = 12, $ND$ = 20). These collective variables have been used by Cascella and Eisenstein to elucidate the Schlenk equilibrium of Grignard reagents.[28–30]

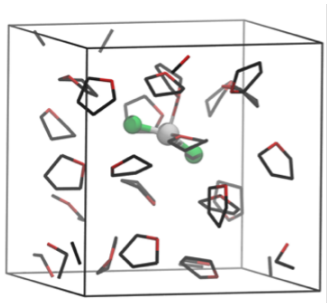

Fig. 2 Example of a periodic cell used for this study. Zn: grey, Cl: green, thf: black and red sticks. H atoms are hidden for clarity.

### Thermodynamic integration in the Blue Moon ensemble

Based on trajectories obtained by *ab initio* metadynamic exploration, a set of structures featuring increasing Zn–O coordination numbers were selected as starting points for individual constrained molecular dynamics simulations. The averaged Lagrange multipliers $\lambda$ were integrated along the Zn–O coordination numbers using the trapezoid rule. To reduce propagation error over integration, the free energy surfaces were split into two equal parts independently integrated and then combined. The error was estimated along the reaction coordinate *via* integration of the standard error on the Lagrangian obtained at each point of the free energy profiles.

### Computation of X-Ray absorption spectroscopic signatures

To validate the combined XANES-MD investigative strategy, we have performed simulations of spectroscopic signatures for each solute using two complementary methods.

*Method A*: 30 structures were randomly selected from the constrained molecular dynamics trajectory at the most stable coordination number. The first solvation shell was kept to compute XAS spectra at the Zn K-edge, which were averaged to produce a computed signature. The XAS signatures were computed using state-selective time-dependent DFT (TD-DFT) as implemented in the ORCA 5.0.4 code.[59] The spectra were computed at the LC-PBE/(def2-SVP H, C|pcSseg-3 Zn|def2-TZVP Cl, O) level of theory that was chosen based on the performance of the range-separated hybrid functional LC-PBE[51,60,61] for TD-DFT,[62,63] and the accuracy of pcSseg basis sets[64] for the description of core electronic density. The Tamm-Dancoff approximation was not used and the exact oscillator strengths were computed. Tighter-than-default integration grid settings (defgrid 3) were defined. The RI-J approximation and COSX numerical integration were used to speed up the calculation of the Coulomb integrals and exact exchange, respectively.[65,66] The def2/J auxiliary basis sets were used in the RI approximations.[67,68] Including zero-order relativistic effects did not further improve simulations. The spectra were convoluted with a variable-width Lorentzian, a method adapted from the convolution method used in the FDMNES code.[69–71] The width $\Gamma$ of the Lorentzian convolution kernel for an absorption ray at an energy $E$ was calculated using **Equation 2**:

$$\Gamma = \Gamma_{\text{Hole}} + \Gamma_{\text{m}} \left[ \frac{1}{2} + \frac{1}{\pi} \arctan\left( \frac{\pi}{3} \frac{\Gamma_{\text{m}}}{E_{\text{Larg}}} \left( e - \frac{1}{e^2} \right) \right) \right] \qquad (2)$$

with $\Gamma_{\text{Hole}} = 1.67\,\text{eV}$ the core-level width of Zn,[72] $\Gamma_{\text{m}} = 5\,\text{eV}$ the maximum width, $E_{\text{Larg}} = 15\,\text{eV}$ the width of the arctangent, and $e = \frac{E - E_{\text{HOMO}}}{E_{\text{Cent}}}$ with $E_{\text{Cent}} = 15\,\text{eV}$ the center of the arctangent, and $E_{\text{HOMO}}$ the energy of the HOMO. This convolution method gave the best agreement with the experimental spectra.

*Method B:* The same level of theory as described in method A was used to compute spectra from structures optimized with Gaussian 9 (rev. D.01),[73] at the following level of theory: M06[74] / def2-TZVP (C, H, O),[75] ECP10MWB with associated basis sets (Zn, Cl)[76,77] / SMD(thf).[78] Incremental increase of the Zn–O distance was used to probe the effect of thf coordination, and relaxed potential energy surface scans were used to investigate the effect of the R–Zn–R' (R, R' = Cl, Me) angles. Ultrafine integration grid settings and tight geometry optimization convergence criteria were used.

## Results and discussion

### Elucidating the solvation states of $ZnCl_2$

$ZnCl_2$ was first considered as a model system for zinc halides in thf. The coordination of up to 4 thf molecules was explored with metadynamics (Figure S2 for preliminary results). The free-energy surface along Zn–O coordination number was then refined by thermodynamic integration. The resulting profile is shown in Figure 3, and its convergence is discussed in Figure S3.

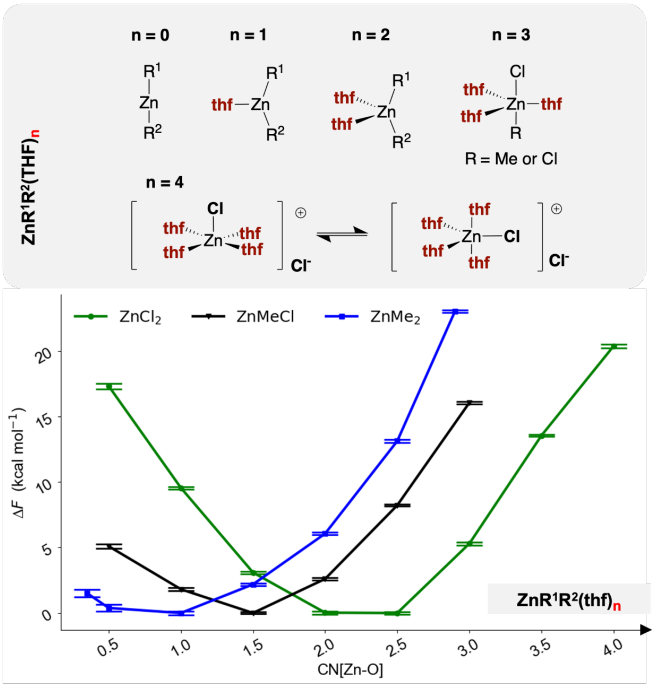


Fig. 3 Helmholtz free energy profile ($\Delta F$) computed for thf coordination to $ZnCl_2$, ZnMeCl, and $ZnMe_2$ and corresponding structures (top).

The most stable forms of $ZnCl_2$ in solution are found for Zn–O coordination numbers $CN[Zn-O]$ of 2.0 and 2.5. These two solvation states are isoenergetic and represent close to 100% of the Boltzmann population at room temperature (Table S3). This is in agreement with the reported XRD structure of $ZnCl_2$ solvated by thf. However, "$ZnCl_2(thf)_2$" as a global minimum does not fully capture the dynamic structure of $ZnCl_2$ in solution as a third thf

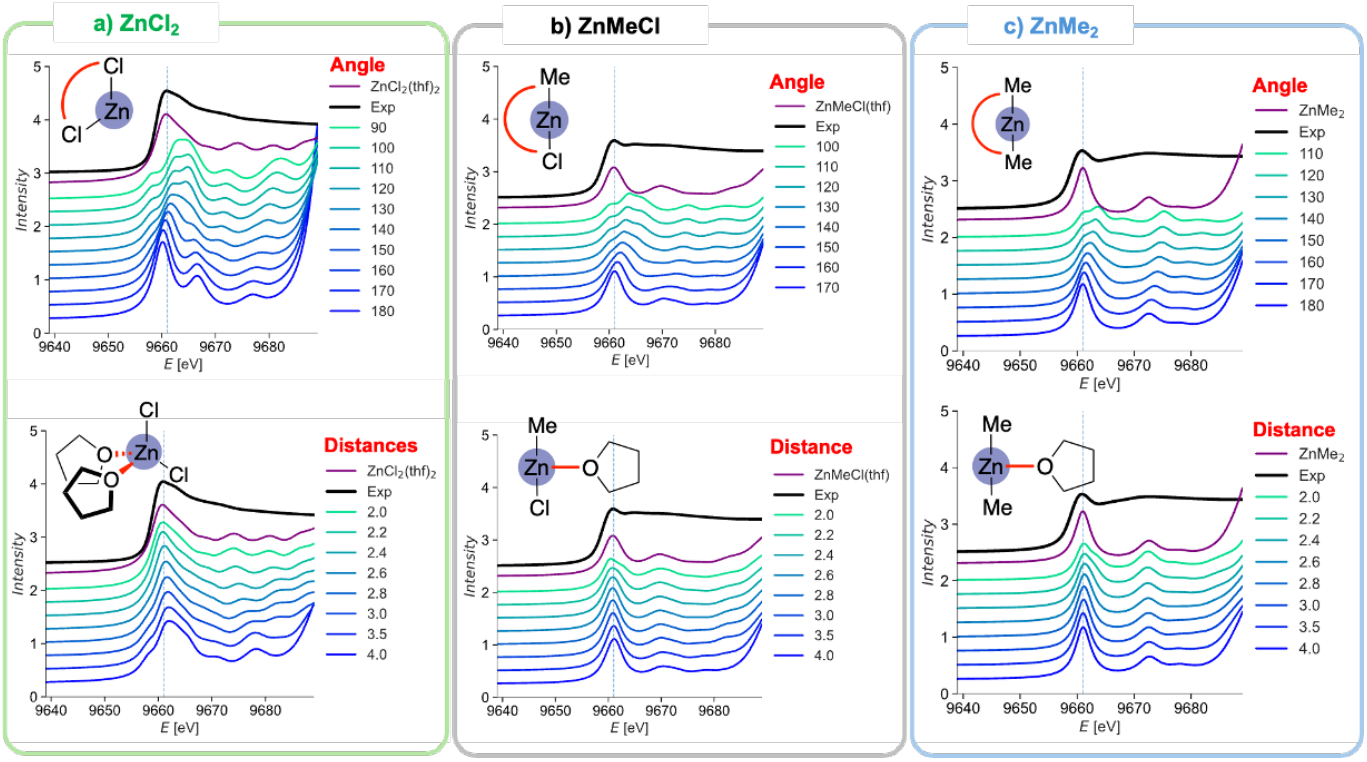


Fig. 4 Comparison between the experimental (black), and the computed XANES spectra for for (a) $ZnCl_2$, (b) ZnMeCl, and (c) $ZnMe_2$. Spectra were computed at the LC-PBE/(def2-SVP H, C | pcSseg-3 Zn | def2-TZVP Cl, O) level of theory, based on 30 frames of the most stable constrained MD trajectory (purple) or with varying R-Zn-R' angles (upper plot, blues and greens) and Zn-O distances (lower plot, blues and greens).

molecule can easily enter the solvation sphere. Although other solvation states of $ZnCl_2$ are less stable, some remain thermodynamically accessible in solution at room temperature. $ZnCl_2(thf)_1$ and $ZnCl_2(thf)_3$ are respectively endergonic by 9.6 and 5.3 kcal $mol^{-1}$ (Figure 3). Solvent induced ionization of $ZnCl_2$ requires the coordination of a $4^{th}$ thf molecule to yield $[ZnCl(thf)_4]^+ \cdot Cl^-$, this equilibrium is endergonic by 20.4 kcal $mol^{-1}$. The resulting cation undergoes fast Berry pseudorotation between its square-based pyramid and trigonal bipyramid forms.

The solvation behavior of $ZnCl_2$ could be confirmed using XANES at the Zn K-edge which was measured for a 1.0 M thf solution of $ZnCl_2$ at 298 K (Figure 4-a-black, detailed procedures and setup in SI). The spectrum exhibits a sharp rising edge at 9659 eV, followed by a whiteline with a maximum at 9661 eV, bearing a prominent shoulder at 9662.5 eV. A spectrum computed from MD trajectories (method A, Figure 4-a-purple) is consistent with the experimental signature. The effect of the Cl–Zn–Cl angle and Zn–O distance(s) over the XANES signature was investigated computationally (method B). Increasing the value of the Cl–Zn–Cl angle from 90° to 180° in non-solvated $ZnCl_2$ reveals that the whiteline shape is best reproduced for a value close to 130° (Figure 4, upper spectrum). The influence of the two thf ligands was then evaluated by increasing the Zn–O distance starting from the optimized structure of $ZnCl_2(thf)_2$ without relaxation. When decoordinating the thf ligands, a shoulder appears in the rising edge region of the spectrum which does not fit the experimental signature. This feature disappears for Zn–O distances below 2.4 Å (Figure 4, lower spectrum). Overall, the spectrum is well reproduced using structures from the constrained molecular dynamics: the whiteline shoulder indicates a bent geometry, while the absence of a rising edge feature indicates thf coordination.

### Elucidating the solvation states of ZnMeCl

From Blue Moon sampling, the most stable solvation state of ZnMeCl is found for $CN[Zn-O] = 1.5$ (Figure 3). This half-integer coordination number indicates that ZnMeCl is in equilibrium between its singly- and doubly-coordinated forms, $ZnMeCl(thf)_2$ being less stable than ZnMeCl(thf) by only 1.8 kcal $mol^{-1}$. The decoordination of a thf molecule from $ZnMeCl(thf)_{1.5}$ to give $ZnMeCl(thf)_{0.5}$ is disfavoured by 5.1 kcal $mol^{-1}$. The coordination of a third thf to yield $ZnMeCl(thf)_3$ is endergonic by 16.0 kcal $mol^{-1}$. Contrary to $ZnCl_2$, the formation of solvent-separated ion pair is was not sampled within an energy range of 16 kcal $mol^{-1}$.

We confronted these simulation results to XANES signatures under standard conditions (Figure 4-b and S6). The experimental spectrum features a sharp rising edge at 9659 eV, a whiteline with a low intensity and two wide bands at 9664 eV and 9670 eV. The spectrum computed from structures sampled by Blue Moon (method A) reproduces a sharp whiteline, but only a single band above the edge. Further investigation of the influence of the structure allow us to probe the reasons for this discrepancy. Increasing Cl–Zn–C angles from 100° to 170° leads to sharper whiteline that better fit with the experimental XANES signature (Figure 4-b upper spectrum). However, the modification of the first solvation

sphere around ZnMeCl does not improve the agreement betwwen computed and simulated spectra at 5 to 10 eV above the edge (Figure 4-b, lower spectrum). This discrepancy can be attributed to the co-existence of pseudo-linear ZnMeCl with other species with lower Cl–Zn–C angles.

### Elucidating the solvation states of $ZnMe_2$

The case of $ZnMe_2$, as a general model for synthetically useful dialkylzinc reagents, deserves particular attention. The global minima is found for $ZnMe_2(thf)$, as shown in Figure 3. Decoordination of a thf ligand from $ZnMe_2(thf)$ to give $ZnMe_2(thf)_{0.5}$ is thermoneutral ($\Delta F$ = 0.3 kcal mol$^{-1}$), suggesting a weakly-bound labile ligand. In contrast, the binding of a second solvent molecule to $ZnMe_2$ is disfavoured by 6.7 kcal mol$^{-1}$. The formation of $ZnMe_2(thf)_3$ from $ZnMe_2(thf)$ can be ruled out at room temperature as it is endergonic by 23.0 kcal mol$^{-1}$.

These predictions regarding $ZnMe_2$ solvation were unambiguously verified using XANES under standard conditions (Figure 4). According to computed spectra (method B), C–Zn–C bending or thf coordination would lead to a shoulder in the whiteline at 1 to 3 eV above the edge. However, this does not rule out the presence of weakly interacting thf molecules further away from the zinc center, as predicted by *ab initio* molecular dynamics as discussed below. Such a solvation state is consistent with the spectrum computed using structures sampled by constrained molecular dynamics (method A). In contrast with the previously reported twofold coordination of thf to $ZnMe_2$ that was supported by IR analyses and calorimetric measurements amended by molecular modelling at the DFT level, a new picture of dialkylzinc solvation by thf arises.[16]

Distinct interpretations of $ZnCl_2$ and $ZnMe_2$ solvation (Figure 3) can be formulated based on the differences in Zn–O distances ($\sim$ 0.4 Å) (Figure S6 and Table S8) and in electron density at the Zn–O bond critical points (0.046 $|e|$) (Figure S10). The shorter bond distance and higher bond critical point electron density for the Zn–O bond(s) in $ZnCl_2(thf)_2$ relative to $ZnMe_2(thf)$ suggest a more covalent ligation of thf to $ZnCl_2$ and a weaker, more dispersion driven, interaction in $ZnMe_2(thf)$ (Tables S5-S6).

## Conclusions

A tailored computational protocol is proposed to elucidate the solvation states of organozinc reagents in solution. Metadynamics and subsequent thermodynamic integration in the Blue Moon ensemble paint a clear picture of solute solvation states. Despite the limitations of EXAFS in differentiating metal–oxygen and metal–carbon bonds, the XANES signature contains relevant information on the symmetry and on the chemical environment around the metal center. Computed XANES signatures based on structures sampled by molecular dynamics were used to assign at the molecular scale the recorded spectra. Overall, the nature of the substituent at the zinc atom has a profound influence on the preferred solvation states in thf solution which are best described by bounded continuums. While the expected doubly coordinated $ZnCl_2(thf)_2$ makes up the largest part of the solvated species, it coexists with a tri-solvated $ZnCl_2$. In the case of $ZnMe_2$, Zn–O coordination numbers ranging from 0 to 1.5 are energetically accessible at ambient temperature, albeit with elongated Zn-O distances, in line with much weaker Zn–thf interactions.

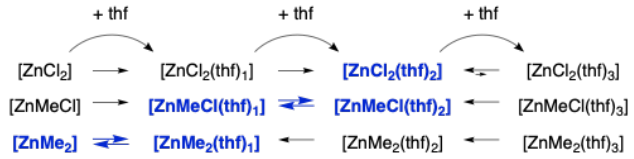


Fig. 5 Overview of the solvation states of zinc compounds in thf solution. The solvation states that ought to be considered as reference for static DFT calculations are highlighted in blue.

Solvent dynamics strongly influences the activity of organozinc reagents. These effects are currently under study, especially regarding transmetallation reactions. When using static DFT calculations for mechanistic investigations, we recommend to first consider the most favourable solvation state, without neglecting the possibility of solvent (de-)coordination along the reaction coordinate. Starting from an unrealistic solvation state will impact the nucleophilicity at the Zn atom, which was shown to have a critical impact on the structure of Zn-Pd bimetallic aggregates,[40] as well as on the free-energy profile of the Pd-catalyzed Negishi cross-coupling.[16]

## Author Contributions

J.R. performed all molecular dynamics simulations and wrote the inital draft. Q.P. prepared the XAS samples, and computed XAS signatures. The acquisition and interpretation of the XAS data was carried out by Q.P. and J.R. The project was designed by P.-A. P. and carried out under the joint supervision of M.-E. L. P. and P.-A. P. All authors contributed to writing the final manuscript.

## Conflicts of interest

There are no conflicts to declare.

## Acknowledgements

All authors would like to thank: O. Eisenstein, C. Raynaud and C. Chizallet for fruitful discussions; O. Safonova and G. Smolentsev from the Paul Scherrer Institut for the design and the implementation of XAS experiments; M. Chen for assisting with XAS measurments; M. Rovezzi from the European Synchrotron Radiation Facility is acknoweldged for his advice on XAS interpretation and simulation; Y. Faugeroux from Faugeroux Mécanique de Précision (Paris, France) for the design and realisation of the PEEK XAS cells. M. C. acknowledges the support of the Research Council of Norway through the Centre of Excellence Hylleraas Centre for Quantum Molecular Sciences (Grant n. 262695), and the Pioneer Research Grant MetalSynergy (Grant n. 314009)

## Notes and references

1 D. Seyferth, *Organometallics*, 2001, **20**, 2940–2955.
2 M. Balkenhohl and P. Knochel, *Chem.–Eur. J.*, 2020, **26**, 3688–3697.
3 B. Baruah and M. L. Deb, *Eur. J. Org. Chem.*, 2021, **2021**, 5756–5766.
4 N. N. Majid M. Heravi, Elaheh Hashemi, *Mol. Diversity*, 2014, **18**, 441–472.
5 D. Haas, J. M. Hammann, R. Greiner and P. Knochel, *ACS Catal.*, 2016, **6**, 1540–1552.
6 J. Rio, L. Perrin and P.-A. Payard, *Eur. J. Org. Chem.*, 2022, **2022**, e202200906.

7 B. Baruah and M. L. Deb, *Eur. J. Org. Chem.*, 2010, **2021**, 5756–5766.
8 H. N. Hunter, N. Hadei, V. Blagojevic, P. Patschinski, G. T. Achonduh, S. Avola, D. K. Bohme and M. G. Organ, *Chem.–Eur. J.*, 2011, **17**, 7845–7851.
9 L. C. McCann, H. N. Hunter, J. A. C. Clyburne and M. G. Organ, *Angew. Chem., Int. Ed.*, 2012, **51**, 7024–7027.
10 L. C. McCann and M. G. Organ, *Angew. Chem., Int. Ed.*, 2014, **53**, 4386–4389.
11 P. Eckert and M. G. Organ, *Chem.–Eur. J.*, 2019, **25**, 15751–15754.
12 P. Eckert, S. Sharif and M. G. Organ, *Angew. Chem., Int. Ed.*, 2021, **60**, 12224–12241.
13 E. M. Hanada, K. Jess and S. A. Blum, *Chem.–Eur. J.*, 2020, **26**, 15094–15098.
14 E. M. Hanada, T. K. S. Tagawa, M. Kawada and S. A. Blum, *J. Am. Chem. Soc.*, 2022, **144**, 12081–12091.
15 E. M. Hanada, P. J. McShea and S. A. Blum, *Angew. Chem., Int. Ed.*, 2023, **62**, e202307787.
16 J. del Pozo, M. Pérez-Iglesias, R. Álvarez, A. Lledós, J. A. Casares and P. Espinet, *ACS Catal.*, 2017, **7**, 3575–3583.
17 J. Zhang, H. Zhang, T. Wu, Q. Wang and D. van der Spoel, *J. Chem. Theory Comput.*, 2017, **13**, 1034–1043.
18 G. Norjmaa, G. Ujaque and A. Lledós, *Top. Catal.*, 2022, **65**, 118–140.
19 S. Halbert and H. Gérard, *Top. Catal.*, 2022, **65**, 481–492.
20 J. P. Guthrie, *J. Phys. Chem. A*, 2001, **105**, 8495–8499.
21 D. Ardura, R. López and T. L. Sordo, *J. Phys. Chem. B*, 2005, **109**, 23618–23623.
22 P. Pracht and S. Grimme, *Chem. Sci.*, 2021, **12**, 6551–6568.
23 A. J. Garza, *J. Chem. Theory Comput.*, 2019, **15**, 3204–3214.
24 A. Laio and M. Parrinello, *Proc. Natl. Acad. Sci. U. S. A.*, 2002, **99**, 12562–12566.
25 C. Michel, A. Laio, F. Mohamed, M. Krack, M. Parrinello and A. Milet, *Organometallics*, 2007, **26**, 1241–1249.
26 O. Valsson, P. Tiwary and M. Parrinello, *Annu. Rev. Phys. Chem.*, 2016, **67**, 159–184.
27 D. Widmer and B. Schwartz, *Nat. Chem.*, 2018, **10**, 910–916.
28 R. M. Peltzer, O. Eisenstein, A. Nova and M. Cascella, *J. Phys. Chem. B*, 2017, **121**, 4226–4237.
29 R. M. Peltzer, J. Gauss, O. Eisenstein and M. Cascella, *J. Am. Chem. Soc.*, 2020, **142**, 2984–2994.
30 M. de Giovanetti, S. H. Hopen Eliasson, A. C. Castro, O. Eisenstein and M. Cascella, *J. Am. Chem. Soc.*, 2023, **145**, 16305–16309.
31 N. Rampal, H.-W. Wang, D. Biriukov, A. B. Brady, J. C. Neuefeind, M. Předota and A. G. Stack, *J. Mol. Liq.*, 2021, **340**, 116898.
32 M. Sprik and G. Ciccotti, *J. Chem. Phys.*, 1998, **109**, 7737–7744.
33 B. Fischer, J. Boersma, G. Van Koten, W. J. J. Smeets and A. L. Spek, *Organometallics*, 1989, **8**, 667–672.
34 M. Weidenbruch, M. Herrndorf, A. Schäfer, S. Pohl and W. Saak, *J. Organomet. Chem.*, 1989, **361**, 139–145.
35 E. Hevia, J. Z. Chua, P. García-Álvarez, A. R. Kennedy and M. D. McCall, *Proc. Natl. Acad. Sci. U. S. A.*, 2010, **107**, 5294–5299.
36 D. R. Armstrong, W. Clegg, P. García-Álvarez, A. R. Kennedy, M. D. McCall, L. Russo and E. Hevia, *Chem.–Eur. J.*, 2011, **17**, 8333–8341.
37 K. Koszinowski and P. Böhrer, *Organometallics*, 2009, **28**, 771–779.
38 J. E. Fleckenstein and K. Koszinowski, *Organometallics*, 2011, **30**, 5018–5026.
39 I. Antes and G. Frenking, *Organometallics*, 1995, **14**, 4263–4268.
40 J. delPozo, E. Gioria, J. A. Casares, R. Álvarez and P. Espinet, *Organometallics*, 2015, **34**, 3120–3128.
41 P. O'Brien, M. B. Hursthouse, M. Motevalli, J. R. Walsh and A. C. Jones, *Journal of Organometallic Chemistry*, 1993, **449**, 1–8.
42 A. Iglesias-Juez, G. L. Chiarello, G. S. Patience and M. O. Guerrero-Pérez, *Can. J. Chem. Eng.*, 2022, **100**, 3–22.
43 G. Zhang, J. Li, Y. Deng, J. T. Miller, A. J. Kropf, E. E. Bunel and A. Lei, *Chem. Commun.*, 2014, **50**, 8709.
44 H. Yi, D. Yang, J. Xin, X. Qi, Y. Lan, Y. Deng, C.-W. Pao, J.-F. Lee and A. Lei, *Nat. Commun.*, 2017, **8**, 14794.
45 V. Migliorati, A. Caruso and P. D'Angelo, *Inorg. Chem.*, 2019, **58**, 14551–14559.
46 R. C. Shiery, J. L. Fulton, M. Balasubramanian, M.-T. Nguyen, J.-B. Lu, J. Li, R. Rousseau, V.-A. Glezakou and D. C. Cantu, *Inorg. Chem.*, 2021, **60**, 3117–3130.
47 D. M. Driscoll, R. C. Shiery, M. Balasubramanian, J. L. Fulton and D. C. Cantu, *Inorg. Chem.*, 2022, **61**, 287–294.
48 T. J. Summers, J. A. Sobrinho, A. de Bettencourt-Dias, S. D. Kelly, J. L. Fulton and D. C. Cantu, *Inorg. Chem.*, 2023, **62**, 5207–5218.
49 R. Bedford and A. Messinis, *Nat. Catal.*, 2018.
50 L. Martínez, R. Andrade, E. G. Birgin and J. M. Martínez, *J. Comput. Chem.*, 2009, **30**, 2157–2164.
51 J. P. Perdew, K. Burke and M. Ernzerhof, *Phys. Rev. Lett.*, 1996, **77**, 3865–3868.
52 J. P. Perdew, A. Ruzsinszky, G. I. Csonka, O. A. Vydrov, G. E. Scuseria, L. A. Constantin, X. Zhou and K. Burke, *Phys. Rev. Lett.*, 2008, **100**, 136406.
53 S. Grimme, J. Antony, S. Ehrlich and H. Krieg, *J. Chem. Phys.*, 2010, **132**, 154104.
54 S. Grimme, S. Ehrlich and L. Goerigk, *J. Comput. Chem.*, 2011, **32**, 1456–1465.
55 T. D. Kühne, M. Iannuzzi, M. Del Ben, V. V. Rybkin, P. Seewald, F. Stein, T. Laino, R. Z. Khaliullin, O. Schütt, F. Schiffmann, D. Golze, J. Wilhelm, S. Chulkov, M. H. Bani-Hashemian, V. Weber, U. Borštnik, M. Taillefumier, A. S. Jakobovits, A. Lazzaro, H. Pabst, T. Müller, R. Schade, M. Guidon, S. Andermatt, N. Holmberg, G. K. Schenter, A. Hehn, A. Bussy, F. Belleflamme, G. Tabacchi, A. Glöß, M. Lass, I. Bethune, C. J. Mundy, C. Plessl, M. Watkins, J. VandeVondele, M. Krack and J. Hutter, *J. Chem. Phys.*, 2020, **152**, 194103.
56 G. Lippert, J. Hutter and M. Parrinello, *Mol. Phys.*, 1997, **92**, 477–488.
57 J. VandeVondele and J. Hutter, *J. Chem. Phys.*, 2007, **127**, 114105.
58 S. Goedecker, M. Teter and J. Hutter, *Phys. Rev. B*, 1996, **54**, 1703–1710.
59 F. Neese, *Wiley Interdiscip. Rev.: Comput. Mol. Sci.*, 2022, **12**,.
60 C. Adamo and V. Barone, *J. Chem. Phys.*, 1999, **110**, 6158–6170.
61 O. A. Vydrov and G. E. Scuseria, *J. Chem. Phys.*, 2006, **125**, 234109.
62 D. Hall, J. C. Sancho-García, A. Pershin, D. Beljonne, E. Zysman-Colman and Y. Olivier, *J. Phys. Chem. A*, 2023.
63 D. Jacquemin, E. A. Perpète, G. E. Scuseria, I. Ciofini and C. Adamo, *J. Chem. Theory Comput.*, 2007, **4**, 123–135.
64 F. Jensen, *J. Chem. Theory Comput.*, 2014, **11**, 132–138.
65 R. Izsák and F. Neese, *J. Chem. Phys.*, 2011, **135**, 144105.
66 F. Neese, F. Wennmohs, A. Hansen and U. Becker, *Chem. Phys.*, 2009, **356**, 98–109.
67 K. Eichkorn, O. Treutler, H. Öhm, M. Häser and R. Ahlrichs, *Chem. Phys. Lett.*, 1995, **240**, 283–290.
68 K. Eichkorn, F. Weigend, O. Treutler and R. Ahlrichs, *Theor. Chem. Acc.*, 1997, **97**, 119–124.
69 O. Bunău and Y. Joly, *J. Phys.: Condens.Matter*, 2009, **21**, 345501.
70 S. A. Guda, A. A. Guda, M. A. Soldatov, K. A. Lomachenko, A. L. Bugaev, C. Lamberti, W. Gawelda, C. Bressler, G. Smolentsev, A. V. Soldatov and Y. Joly, *J. Chem. Theory Comput.*, 2015, **11**, 4512–4521.
71 J. D. Bourke, C. T. Chantler and Y. Joly, *J. Synchrotron Radiat.*, 2016, **23**, 551–559.
72 M. O. Krause and J. H. Oliver, *J. Phys. Chem. Ref. Data*, 1979, **8**, 329–338.
73 M. J. Frisch, G. W. Trucks, H. B. Schlegel, G. E. Scuseria, M. A. Robb, J. R. Cheeseman, G. Scalmani, V. Barone, B. Mennucci, G. A. Petersson, H. Nakatsuji, M. Caricato, X. Li, H. P. Hratchian, A. F. Izmaylov, J. Bloino, G. Zheng, J. L. Sonnenberg, M. Hada, M. Ehara, K. Toyota, R. Fukuda, J. Hasegawa, M. Ishida, T. Nakajima, Y. Honda, O. Kitao, H. Nakai, T. Vreven, J. A. Montgomery, Jr., J. E. Peralta, F. Ogliaro, M. Bearpark, J. J. Heyd, E. Brothers, K. N. Kudin, V. N. Staroverov, R. Kobayashi, J. Normand, K. Raghavachari, A. Rendell, J. C. Burant, S. S. Iyengar, J. Tomasi, M. Cossi, N. Rega, J. M. Millam, M. Klene, J. E. Knox, J. B. Cross, V. Bakken, C. Adamo, J. Jaramillo, R. Gomperts, R. E. Stratmann, O. Yazyev, A. J. Austin, R. Cammi, C. Pomelli, J. W. Ochterski, R. L. Martin, K. Morokuma, V. G. Zakrzewski, G. A. Voth, P. Salvador, J. J. Dannenberg, S. Dapprich, A. D. Daniels, O. Farkas, J. B. Foresman, J. V. Ortiz, J. Cioslowski and D. J. Fox, *Gaussian 09 Revision E.01*, Gaussian Inc. Wallingford CT 2009.
74 Y. Zhao and D. G. Truhlar, *Theor. Chem. Acc.*, 2008, **120**, 215–241.
75 F. Weigend and R. Ahlrichs, *Phys. Chem. Chem. Phys.*, 2005, **7**, 3297–3305.
76 M. Dolg, U. Wedig, H. Stoll and H. Preuss, *J. Chem. Phys.*, 1987, **86**, 866–872.
77 J. M. Martin and A. Sundermann, *J. Chem. Phys.*, 2001, **114**, 3408–3420.
78 A. V. Marenich, C. J. Cramer and D. G. Truhlar, *J. Phys. Chem. B*, 2009, **113**, 6378–6396.